

# Comparison of Aerodynamic Characterization Methods for Design of Unmanned Aerial Vehicles

Or D. Dantsker \*

Moiz Vahora<sup>†</sup>

*Al Volo LLC, Urbana, IL 61801*

*University of Illinois at Urbana-Champaign, Urbana, IL 61801*

Attaining accurate predictions for the aerodynamic characteristics of a potential aircraft design is vital in the preliminary design process. Additionally, determining the aerodynamic characteristics of an existing aircraft is just as important. In both these cases, obtaining aerodynamic characteristics, such as the lift, drag, and moment curves is essential for determining aircraft stability and performance. The prediction methods should both yield accurate results as well as be computationally inexpensive. This paper discusses and compares several computational tools used to determine the aerodynamic characteristics of an unmanned aircraft with experimental results obtained from flight testing. Two low-order computational tools based on lifting-line theory, XFLR5 and AVL, as well as one high-order method, using the computational fluid dynamics tool Ansys Fluent, were used. The example aircraft used was a 62.5 in wingspan fixed-wing unmanned aircraft, which had previously been 3D scanned. The 3D scan point cloud was processed to produce detailed geometry data that was input into the computational tools. Results from the computational tools and flight testing for the longitudinal stability of the aircraft are presented and compared.

## Nomenclature

<i>CAD</i>	=	computer aided design
<i>CFD</i>	=	computational fluid dynamics
<i>GPS</i>	=	global positioning system
<i>IMU</i>	=	inertial measurement unit
<i>NLLT</i>	=	non-linear lifting line theory
<i>Re</i>	=	Reynolds number
<i>RC</i>	=	radio control
<i>UAV</i>	=	unmanned aerial vehicle
<i>VLM</i>	=	vortex lattice method
$a_x, a_y, a_z$	=	body-axis translational acceleration
$c$	=	wing mean chord
$C_l, C_d, C_m$	=	lift, drag, and moment coefficient for airfoil
$C_L, C_D, C_M$	=	lift, drag, and moment coefficient for aircraft
$C_{L_\alpha}, C_{D_\alpha}, C_{M_\alpha}$	=	lift, drag, and moment curve slope for aircraft
$C_{L_0}, C_{D_0}, C_{M_0}$	=	lift, drag, and moment coefficient at zero angle-of-attack for aircraft
$D$	=	drag
$L$	=	lift
$m$	=	aircraft mass
$P$	=	static pressure
$p, q, r$	=	roll, pitch and yaw rotation rates
$\dot{p}, \dot{q}, \dot{r}$	=	roll, pitch and yaw angular accelerations
$S$	=	wing area
$u, v, w$	=	body-fixed true velocity

\*Aero-Mechanical Engineer. ordantsker@alvolo.us

<sup>†</sup>M.S. Student, Department of Aerospace Engineering, AIAA Student Member. mvahor2@illinois.edu

$v_x, v_y, v_z$	=	inertial-fixed ground velocity in ENU coordinate system
$V$	=	total speed
$x, y, z$	=	inertial-fixed position in ENU coordinate system
$\alpha$	=	angle-of-attack
$\beta$	=	sideslip angle
$\phi, \theta, \psi$	=	roll, pitch and heading angles
$\rho$	=	density of air

## I. Introduction

Attaining accurate predictions for the aerodynamic characteristics of a potential aircraft design is vital in the preliminary design process. Additionally, determining the aerodynamic characteristics of an existing aircraft is just as important. In both these cases, obtaining aerodynamic characteristics, such as the lift, drag, and moment curves is essential for determining aircraft stability and performance. The prediction methods should both yield accurate results and be computationally inexpensive. Two low-order computational tools that offer rapid results and are widely used are XFLR5<sup>1</sup> and Athena Vortex Lattice (AVL).<sup>2</sup> AVL employs an extended vortex lattice model to generate the lifting surface and it can also implement a slender body to model the fuselage.<sup>2</sup> XFLR5 can use a variety of analysis tools, such as lifting line theory, vortex lattice method (VLM), and 3D panels,<sup>1</sup> where viscous calculations can be interpolated from XFOIL data.<sup>3</sup>

Alternatively, one could also determine the aerodynamic characteristics of an unmanned aircraft design using a high-order method, e.g. using a computational fluid dynamics (CFD) tool such as Ansys Fluent. The most intensive and expensive process for determining characteristics is through flight testing, which is impractical for preliminary design. Both of these options are significantly more expensive in terms of man-hours and cost.

This paper discusses and compares the computational tools, XFLR5 and AVL, as well as the CFD tool, Ansys Fluent, in the context of unmanned aircraft design. The computational tools were used to determine the aerodynamic characteristics of an unmanned aircraft, which were compared with experimental results obtained from flight testing. The example aircraft used is a 62.5 in. wingspan fixed-wing unmanned aircraft, which had previously been 3D scanned.<sup>4</sup> The 3D scan point cloud was processed to produce detailed geometry data that was input into the computational solvers.

This paper will first examine the computational tools as well as flight testing used to determine the aerodynamic characteristics of an aircraft. Then, 3D scan data and resulting geometry will be presented. After that, the longitudinal stability results from the low-order computational tools, high-order CFD tool, and flight test will be presented and compared. Finally conclusions and future work will be discussed.

### A. Review of Low-Order Computational Methods to Determine Aircraft Aerodynamics

Low order tools such as XFLR5 and AVL are often used in the preliminary design process to determine the aerodynamic characteristics of aircraft. XFLR5 and AVL require very little computational time in comparison to CFD solvers and they can produce accurate results. Though low order tools are useful and inexpensive to use, the user should understand the limitations of the analysis conducted before concluding their study.

XFLR5 has three analysis tools used for aerodynamic analysis, consisting of the non-linear lifting line theory (NLLT), vortex lattice method (VLM), and 3D panels. NLLT approximates the wing as a lifting line, which limits the analysis to one lifting surface, but it can incorporate viscous effects interpolated from XFOIL data. VLM models the lifting surface as a discrete number of vortices, which can be used to analyze the wing and tail surfaces. The VLM formulation assumes a small angle-of-attack and the viscous results from the analysis are obtained from interpolating  $C_l$  from the airfoil lift curve, meaning that results near stall should not be considered.<sup>5</sup> The 3D panel method takes into account the thickness of the wing using a doublet and sources, allowing the user to calculate the pressure distribution.<sup>6</sup> The viscous results from the 3D panel method are determined by interpolating  $C_l$  from the airfoil like the VLM implementation, though analysis is constrained to a single lifting surface.<sup>1</sup>

AVL uses a vortex lattice method to determine aerodynamic coefficients for small angles-of-attacks and sideslips. The computations obtained from AVL are inviscid, limiting the scope of the analysis from a

performance standpoint. One of the main advantages of AVL is the implementation of a fuselage body into the analysis of the aircraft. AVL models the fuselage section of the aircraft using sources and doublet filaments using slender body theory, where each cross section of the fuselage is modeled as a circle with an area equal to the corresponding fuselage section<sup>2</sup>

## B. Review of Flight Testing to Determine Aircraft Aerodynamics

Researchers typically determine the aerodynamic characteristics of an unmanned aircraft using two types of experimental methods. In both cases, they flight test the aircraft and either collect flight data using on-board sensors or externally using a motion capture system. There are a handful of examples for both methods.

On-board data collection requires an aircraft to carry a logging device and sensors, which increases the weight of the aircraft and thereby limits what aircraft can be flight tested this way. Researchers at the University of Florida used a small outdoor aerobatic unmanned aircraft to investigate high angle-of-attack flight dynamics, which included stability issues that related to sideslip<sup>7</sup> and wing rock;<sup>8-10</sup> the aircraft they used had all sensors and recording equipment on board. Researchers at NASA Ames Research Center and Langley Research Center have used a variety of instrumented aircraft to record flight data.<sup>11-13</sup> Further work has also occurred at the University of Kansas<sup>14-18</sup> and the University of Illinois.<sup>19-23</sup>

In terms of using a motion capture system to capture aerodynamics data, state data is collected externally using motion capture systems set in indoor flying spaces with no wind. There is an inherent limitation that comes from the size of the flying space and the number of cameras available for that capture volume, so an aircraft must be below a certain size. This methods was used by researchers at the Georgia Institute of Technology, where a miniature indoor aerobatic aircraft was used to demonstrate a guidance controller for transitions into hovering state.<sup>24</sup> Similar work was done at the Massachusetts Institute of Technology<sup>25</sup> and Universit Laval.<sup>26</sup> Using a comparable motion capture system, researchers at the University of Illinois parametrized a micro, aerobatic aircraft to determine its aerodynamic characteristics including lift, drag, and moment curves over a wide flight regime.<sup>27</sup>

## II. 3D Scanning and Aircraft Geometry Data

The 3D scanning was performed using a ZCorporation ZScanner 800 self-positioning handheld 3D scanner.<sup>4,28</sup> The aircraft used was a 62.5 in wingspan fixed-wing UAV, which was based on Great Planes Avistar Elite.<sup>29</sup> The same aircraft has previously been used to test a sensor data acquisition system.<sup>21,30</sup> The aircraft was instrumented with an AI Volo FDAQ data acquisition system.<sup>31</sup> The completed flight-ready aircraft is shown in Fig. 1, its physical specifications are given in Table 1, and its airframe component specifications are given in Table 2.

The 3D point cloud output from the scanner was processed using a previously written MATLAB script called AirplaneScan. The 3D scan pointcloud of the Avistar UAV was translated and rotated from its original skewed angle and location. The tip of the nosecone was placed at the origin with the x-axis toward the left, the y-axis out the tail, and the z-axis up; it should be noted that a non-standard coordinate system is used. The points on the right half of the airplane were discarded, and then the points on the left half were mirrored to the right with the exception of the nose gear, which was not mirrored. The resulting processed 3D point cloud can be seen in a 3-view and an isometric view in Fig. 2. The processed point cloud was then sliced multiple times to yield the cross sections of the fuselage, wings, and tail sections; the points were plotted in Figs. 3-6.

The pointcloud slices generated by the AirplaneScan MATLAB script provided dimensions and coordinates for all of the flight surfaces. It is important to note that the wing has a constant airfoil throughout the span and the horizontal and vertical stabilizers each have continuously varying airfoils from root to tip. The coordinates of each airfoil produced are plotted in Fig. 7. The wing airfoil coordinates were previously verified<sup>4</sup> with coordinates for the AVISTAR airfoil found on the UIUC Airfoil Database<sup>32</sup> and the stabilizer airfoils were verified with manual measurements. The dimensions of each flight surface and the airfoil locations are given in Table 3; the coordinate system used has the x-axis towards the tail, the y-axis towards the right wing, and the z-axis up. Using the fuselage geometry from the 3D scan and the aforementioned flight surface geometry, a computer aided design (CAD) model of the aircraft was made in SolidWorks (see Fig. 8).



Figure 1. Great Planes Avistar Elite model aircraft.

Table 1. Great Planes Avistar Elite model aircraft physical specifications.

Geometric Properties	
Overall Length	55.0 in (1395 mm)
Wing Span	62.5 in (1590 mm)
Wing Area	672 in <sup>2</sup> (43.3 dm <sup>2</sup> )
Aspect Ratio	6.62
Inertial Properties	
Weight	
Empty (w/o Battery)	7.53 lb (3.415 kg)
4S LiPo Battery	1.17 lb (0.530 kg)
Gross Weight	8.70 lb (3.945 kg)
Wing Loading	29.8 oz/ft <sup>2</sup> (90.9 gr/dm <sup>2</sup> )

Table 2. Great Planes Avistar Elite model aircraft airframe component specifications.

Construction	Built-up balsa and plywood structure, aluminum wing tube, aluminum landing gear, abs canopy, and plastic film sheeted.
Flight Controls	
Controls	Aileron (2), elevator, rudder, throttle, and flaps (2)
Transmitter	Futaba T14MZ
Receiver	Futaba R6014HS
Servos	(6) Futaba S3004
Regulator Distribution	Castle Creations CC BEC
Receiver Battery	Thunder ProLite 20c 2S 7.4V 450 mAh
Propulsion	
Motor	AXI 4120/14 Outrunner
ESC	Castle Creation Phoenix ICE 75 Amp Brushless Speed Controller
Propeller	APC 13x8E
Motor Flight Pack	Thunder Power ProPower 30c 4S 14.8 V 5 Ah lithium polymer battery
Flight Time	10-20 min

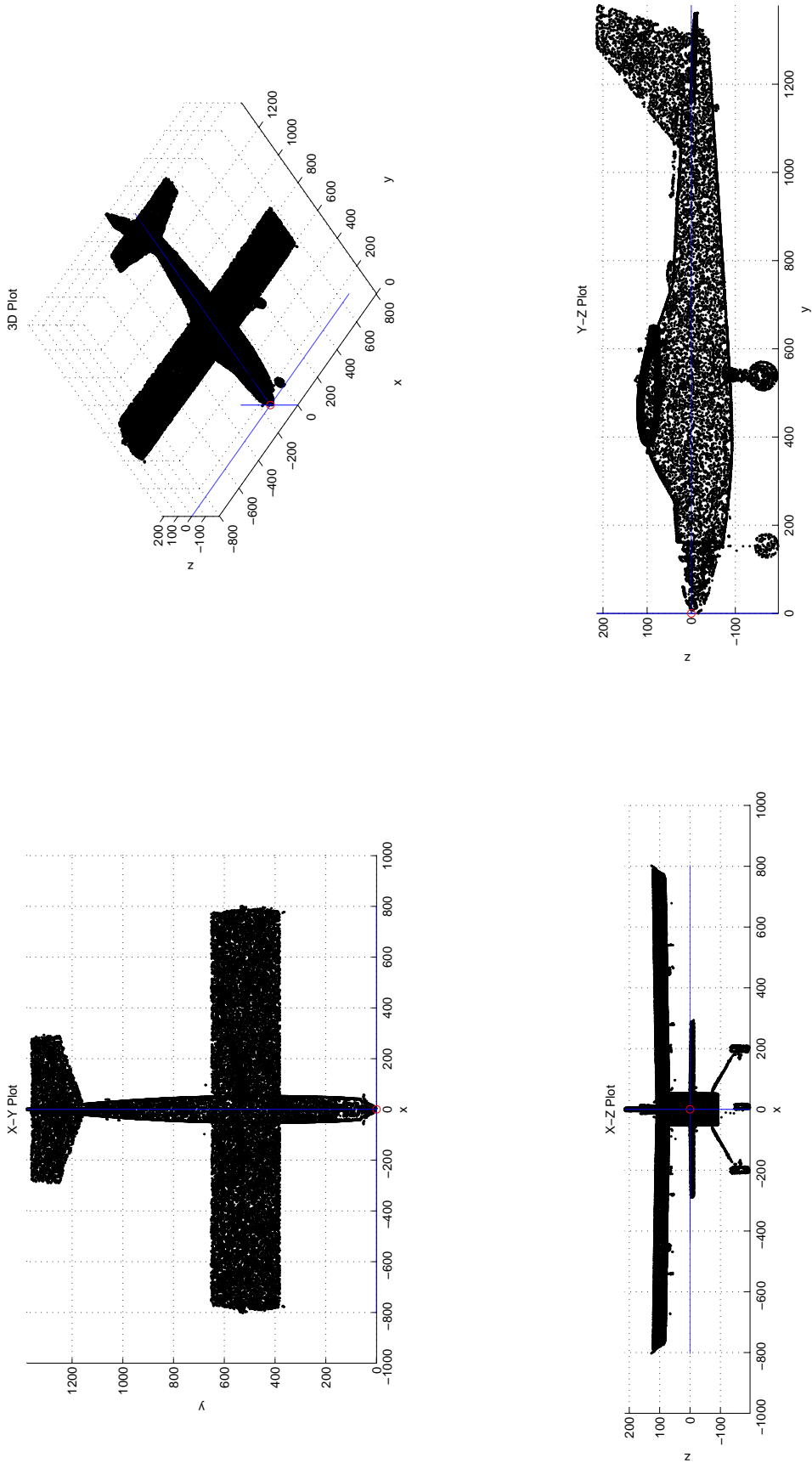


Figure 2. 3-view and isometric plots of the Avistar UAV scan after processing.

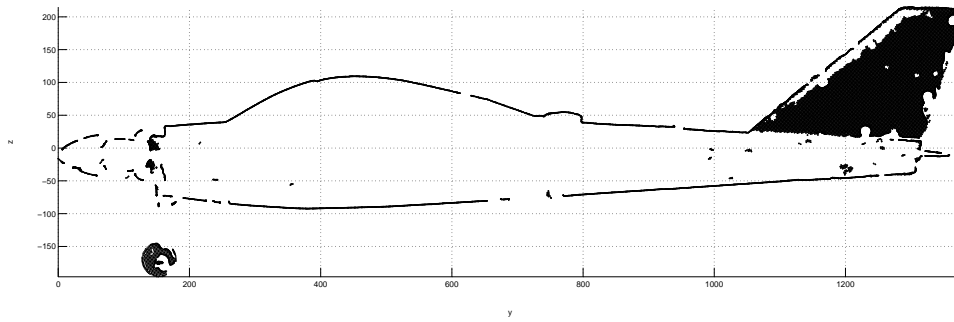


Figure 3. Plot of Y-Z slice of the 3D scan point cloud between  $x=-5$  and  $x=5$ .

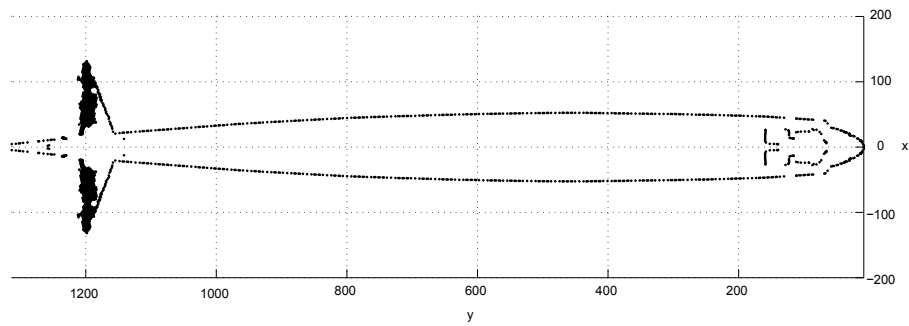


Figure 4. Plot of X-Y slice of the 3D scan point cloud between  $z=0$  and  $z=1$ .

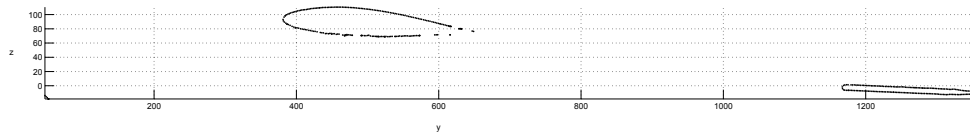


Figure 5. Plot of Y-Z slice of the 3D scan point cloud between  $x=53$  and  $x=55$ .

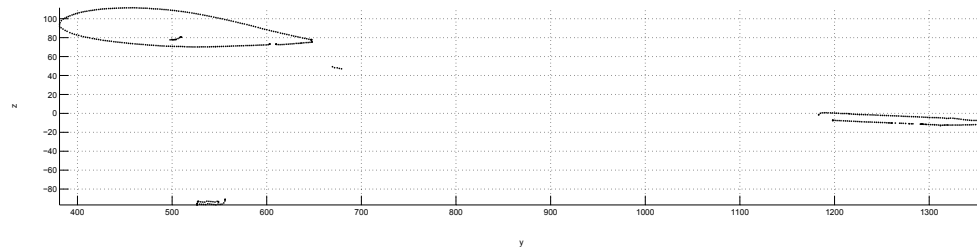


Figure 6. Plot of Y-Z slice of the 3D scan point cloud between  $x=98$  and  $x=100$ .

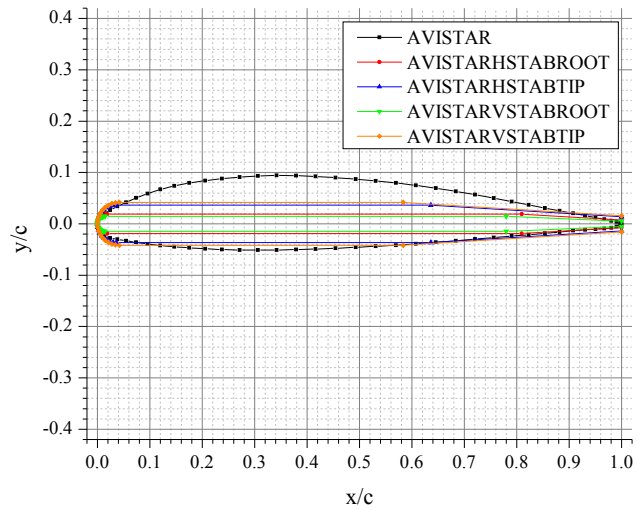


Figure 7. The airfoils used on the Avistar UAV.

Table 3. Avistar UAV flight surface specifications.

Wing							
LE x pos	LE z pos	Incidence	y span pos	Chord	Offset	Dihedral	Airfoil
380.4 mm	95.5 mm	3.58 deg	0 mm	237.10 mm	0 mm	0.9 deg	AVISTAR
-	-	-	793.75 mm	237.10 mm	0 mm	-	AVISTAR
Horizontal Stabilizer							
LE x pos	LE z pos	Incidence	y span pos	Chord	Offset	Dihedral	Airfoil
1160 mm	-2.04 mm	2.36 deg	0 mm	210 mm	0 mm	0 deg	AVISTARHSTABROOT
-	-	-	291 mm	110 mm	100 mm	-	AVISTARHSTABTIP
Vertical Stabilizer							
LE x pos	LE z pos	Incidence	y span pos	Chord	Offset	Dihedral	Airfoil
1160 mm	17.96 mm	2.36 deg	0 mm	273 mm	-95 mm	0 deg	AVISTARVSTABROOT
-	-	-	200 mm	96 mm	133 mm	-	AVISTARVSTABTIP

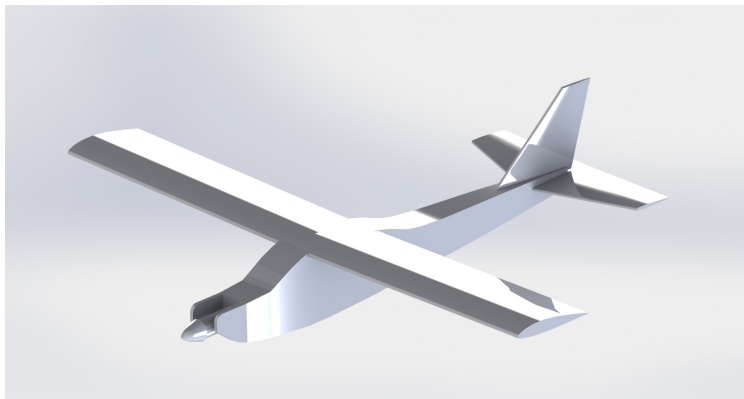


Figure 8. A SolidWorks CAD model of the Avistar UAV.

### III. Low-Order Tools

#### A. XFRLR5

The aircraft geometry generated by the 3D scan, described in Section II, was implemented into the aerodynamics analysis tool, XFRLR5. XFRLR5 is based on XFOIL's<sup>3</sup> analysis capabilities and uses Lifting Line Theory, Vortex Lattice Method, and 3D Panel Method to generate results. As mentioned earlier, the program has a few drawbacks including not being able to model fuselages well and only being able to use Vortex Lattice Method on aircraft (wings and tail surfaces) as opposed to just the wing where all three methods are available. This problem is well documented by the XFRLR5 authors.<sup>33</sup>

The airfoil coordinates and flight surface location were entered into XFRLR5, and the resultant model can be seen in Fig. 9. The fuselage was withheld from the aerodynamics model per recommendations provided in the documentation of XFRLR5, as mentioned earlier. In order to test the aerodynamics model in XFRLR5, each of the airfoils needed to be run for all possible Reynolds numbers and angles-of-attack. The Reynolds number was swept between 10,000 and 500,000 and the angle-of-attack was swept between -15 deg and 15 deg, to provide the greatest possible operating range for both the wing and stabilizers. XFRLR5 was used to run the Avistar aerodynamics model for a flight speed of 14 m/s (46 mph) in inviscid mode—see the polars in Fig. 10.

XFRLR5 was only able to produce results between angles-of-attack of -4 and 10 deg. Beyond these angles, XFRLR5 was unable to interpolate between the airfoil performance curves. As mentioned earlier, XFRLR5 only allows for aircraft models to be run using VLM, which produces results that are not quite viscous and therefore cannot capture stall. The inviscid method produced results for the entire angle-of-attack range; however, it failed to produce accurate drag predictions due to a lack of viscous effects and accurate stall predictions.

From the results, angles-of-attack of  $\pm 4$  deg, the aircraft stability derivatives  $C_{L_\alpha}$ ,  $C_{D_\alpha}$ , and  $C_{M_\alpha}$  were found. In Fig. 10, the lift, drag, and moment coefficients for a flight speed of 14 m/s were plotted against angle-of-attack, and these points are fitted linearly. The linear fittings, which were performed within the angle-of-attack of  $\pm 4$  deg, produced slopes for each curve which are equal to the stability derivatives. It should be noted that this is not a standard method for calculating the drag stability derivative, however, since the standard method relies on knowing the Oswald efficiency factor, which was assumed to not be known a priori. We revert to using the linear fitting in a slightly parabolic range; the non-standard method for finding the drag term provides us a good first order approximation. The values of the stability derivatives produced are:

$$\begin{aligned} C_{L_\alpha} &= 0.0827 & C_{L_0} &= 0.357466 \\ C_{D_\alpha} &= 0.0075 & C_{D_0} &= 0.020282 \\ C_{M_\alpha} &= -0.0249 & C_{M_0} &= -0.00799 \end{aligned}$$

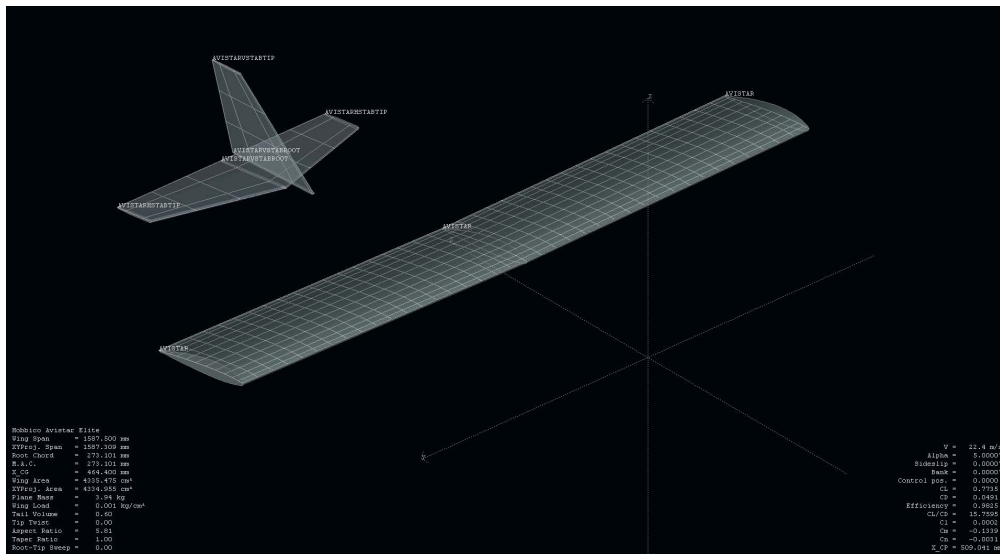


Figure 9. XFRLR5 aerodynamics model for the Avistar UAV.

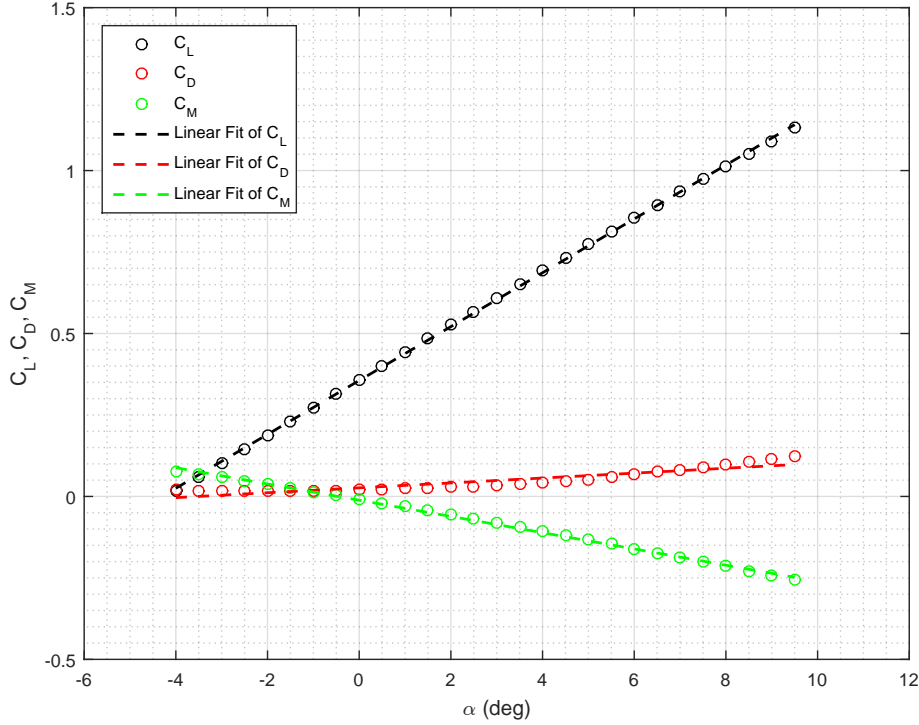


Figure 10. XFLR5 lift, drag, and moment coefficients vs. angle-of-attack for the Avistar UAV at 14 m/s.

## B. AVL

The aircraft geometry generated by the 3D scan, described in Section II, was implemented into the aerodynamics analysis tool, AVL. The fuselage geometry was created using the 3D scan point cloud. The area of each fuselage section along the length was calculated and a circular cross section of equivalent area was implemented into AVL for the analysis. The same flight speeds mentioned in section A were used for the analysis. The analyzed geometry is given in Fig. 11. As mentioned in Section I, AVL is an inviscid analysis, meaning that viscous effects are not taken into account for the aerodynamic analysis of the Avistar. Though viscous effects are not taken into account, the fuselage can be included in the analysis, allowing the user to calculate how it can effect the stability derivatives.

From the AVL analysis, angles-of-attack of  $\pm 4$  deg were analyzed and the aircraft stability derivatives  $C_{L_\alpha}$ ,  $C_{D_\alpha}$ , and  $C_{M_\alpha}$  were found. This range of angles-of-attack were chosen because AVL is designed to analyze aircraft configurations at low angles-of-attack.<sup>2</sup>The lift, drag, and moment coefficients for a flight speed of 14 m/s were plotted against angle-of-attack, and these points were fit linearly as shown in Fig. 12. The linear fittings, which were performed within the angle-of-attack range of  $\pm 6$  deg, produced slopes for each of the curves, which are equal to the stability derivatives. The values of the stability derivatives produced are:

$$\begin{aligned}
 C_{L_\alpha} &= 0.0810 & C_{L_0} &= 0.33088 \\
 C_{D_\alpha} &= 0.0043 & C_{D_0} &= 0.00633 \\
 C_{M_\alpha} &= -0.0193 & C_{M_0} &= -0.06364
 \end{aligned}$$

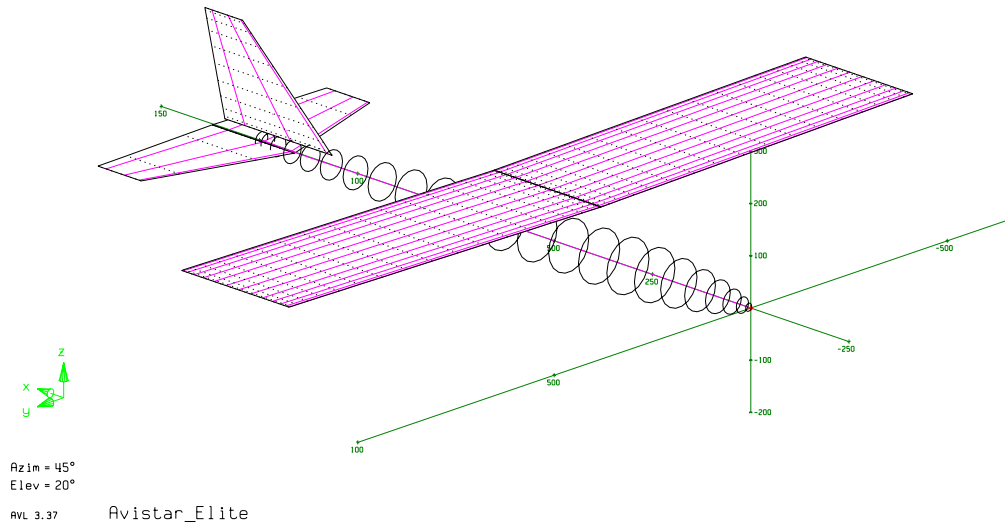


Figure 11. AVL aerodynamics model for the Avistar UAV.

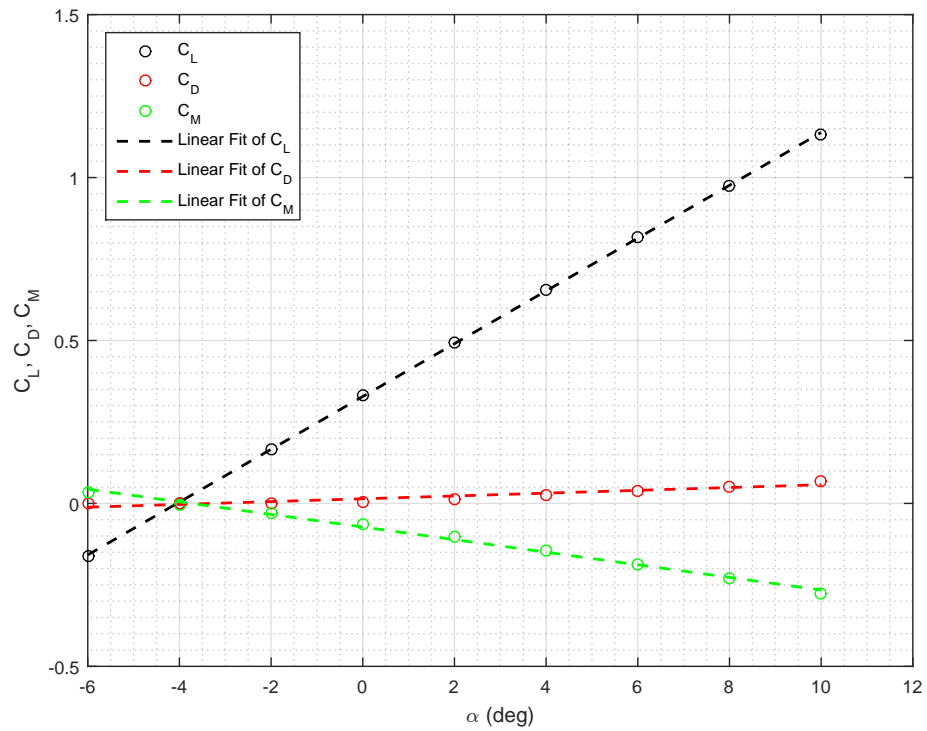


Figure 12. AVL lift, drag, and moment coefficients vs. angle-of-attack for the Avistar UAV at 14 m/s.

## IV. High-Order Tool

A CFD simulation was performed using Ansys Fluent.<sup>34</sup> Using the CAD model described in Section II, a mesh was created using the Fluent meshing tool with 4 million cells, as shown in Fig. 13. The CFD simulation used a with K-epsilon ( $k-\epsilon$ ) turbulence model and was run on an 18-core Intel Xeon Processor E5-2697 v4 workstation with 32 GB DDR4 and a 4 GB GDDR5 NVIDIA Quadro K4200, which has 1344-CUDA cores. The freestream velocity of the analysis was 14 m/s, which operated under standard atmospheric conditions.

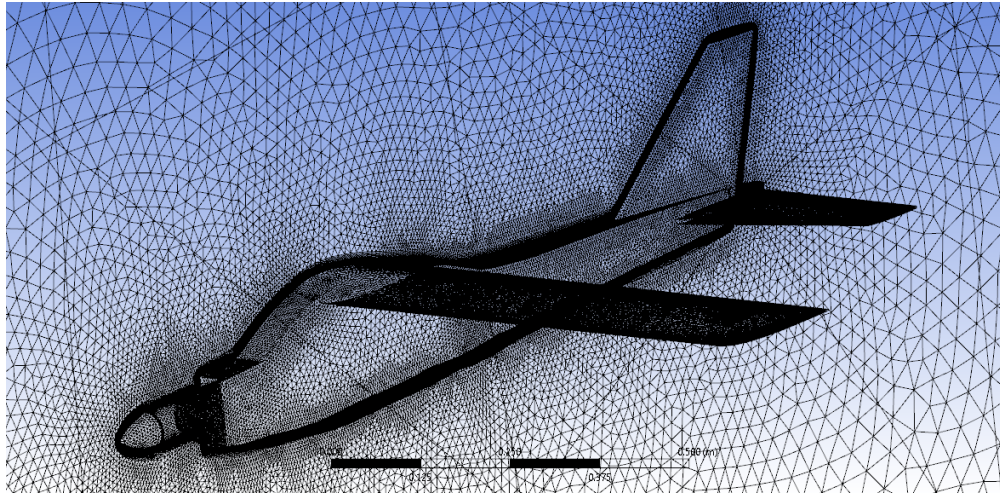


Figure 13. Avistar UAV CAD model meshed in Ansys Fluent with 4 million cells.

The analysis was conducted for angles-of-attack from -4 to 14 deg, with increments of 2 deg. Fig. 14 shows the lift and drag coefficients for each of the runs. Ansys Fluent predicted that aircraft stalls at approximately 10 to 12 deg and thus the stability derivatives were calculated using data from -4 to 8 deg, which appear linear. The stability derivatives are tabulated below.

$$\begin{array}{ll} C_{L_\alpha} = 0.0667 & C_{L_0} = 0.3875 \\ C_{D_\alpha} = 0.0067 & C_{D_0} = 0.05512 \\ C_{M_\alpha} = -0.0340 & C_{M_0} = -0.00659 \end{array}$$

Streamlines for the wing, tail, and fuselage from the CFD analysis are shown in Figs. 15, 16, and 17, respectively. Warmer colors in the streamline figure indicate higher speeds while cooler colors show lower speeds. As seen, the flow is fully attached on the wing. At 4 deg, warmer shades of streamlines indicate higher flow acceleration compared to 10 and 14 deg. Beyond stall at 14 deg, flow separation was observed near the root while the flow is attached near the tip. This shows that the onset of stall begins near the hub region instead of the tip. Flow streamlines are attached on the tail until 10 deg but large separation can be observed for 14 deg. There is also a significant spanwise flow near the root of the horizontal tail at 14 deg. This is due the interference from the flow from the fuselage as shown below. Similarly, at lower angles-of-attack (4 deg), the flowfield is primarily two-dimensional on the fuselage. However, at higher angles-of-attack (14 deg) the flow becomes highly three-dimensional due to flow separation from the fuselage.

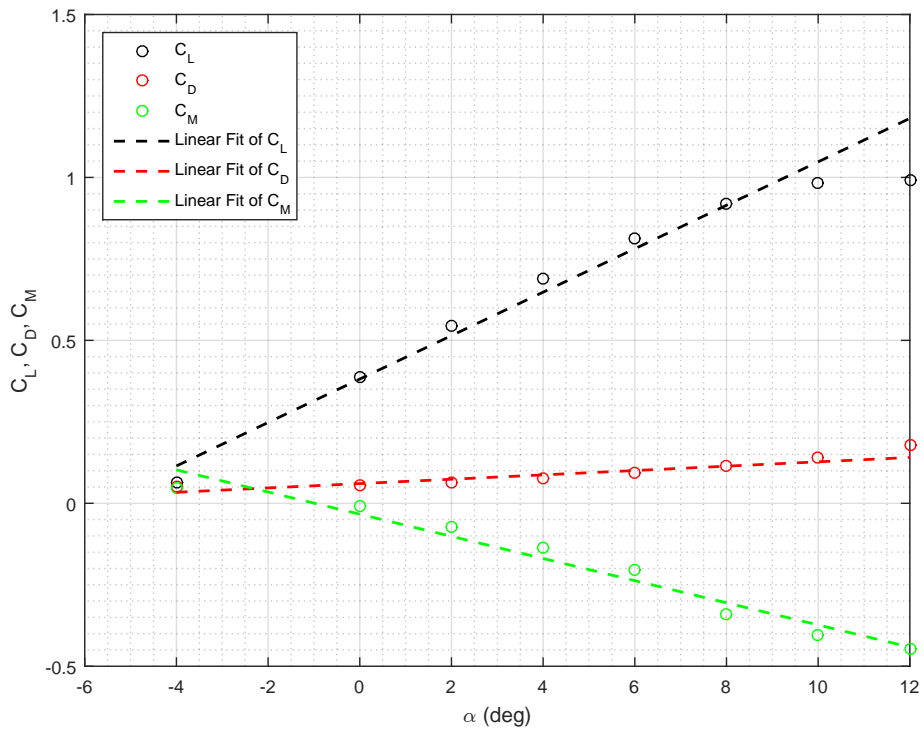


Figure 14. Ansys Fluent lift and drag coefficients vs. angle-of-attack for the Avistar UAV at 14 m/s.

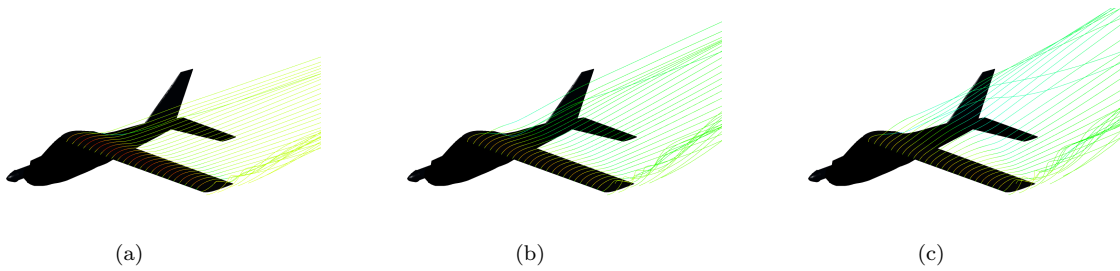


Figure 15. Wing streamlines from Ansys Fluent at angles-of-attack of: (a) 4 deg, (b) 10 deg, and (c) 14 deg.

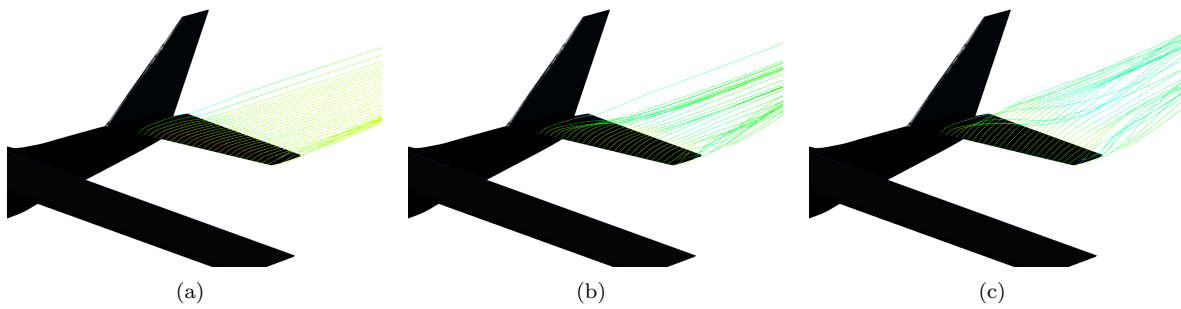


Figure 16. Tail streamlines from Ansys Fluent at angles-of-attack of: (a) 4 deg, (b) 10 deg, and (c) 14 deg.

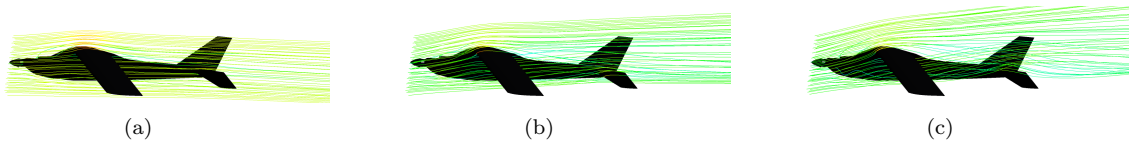


Figure 17. Fuselage streamlines from Ansys Fluent at angles-of-attack of: (a) 4 deg, (b) 10 deg, and (c) 14 deg.

## V. Flight Testing

### A. Setup

The Avistar UAV was re-instrumented for flight testing with an Al Volo FDAQ data acquisition system. The performance specifications of the instrumentation used for flight testing are given in Table 4 and the component specifications are given in Table 5. The aircraft was flight tested during the summer of 2017.

**Table 4. Performance specifications of the instrumentation.**

<b>Sensors</b>	
<b>Inertial sensors</b>	3-axis, $\pm 5$ g accelerometer 3-axis, $\pm 300$ deg/s gyroscope
<b>Magnetometers</b>	3-axis $\pm 750$ mG and 3-axis $\pm 11$ G
<b>Altimeter (barometric)</b>	1 ft resolution
<b>Airspeed (pitot probe)</b>	5–120 mph, 0.1 mph resolution
<b>GPS position</b>	Up to 400 Hz (IMU assisted)
<b>Tachometer</b>	Motor ESC based
<b>PWM inputs</b>	Up to 22
<b>Analog inputs</b>	Up to 32x 0-5V 12 bit
<b>Data Handling</b>	
<b>Rate</b>	400 Hz
<b>Storage</b>	32 GB
<b>Local output</b>	Serial or Ethernet
<b>RF link</b>	900 MHz

**Table 5. Component specifications of the instrumentation.**

<b>Data acquisition system</b>	Al Volo FDAQ 400 Hz system
<b>Inertial and Flow Sensors</b>	
<b>Inertial measurement unit</b>	XSens MTi-G-700 AHRS with GPS
<b>Airspeed probe</b>	EagleTree Systems pitot-static probe
<b>Airspeed sensor</b>	All Sensors 20cmH2O-D1-4V-MINI differential pressure sensor
<b>Motor Sensors</b>	Castle Creations Serial Link connected to FDAQ motor sensor input
<b>Power</b>	
<b>Regulator</b>	Built into FDAQ
<b>Battery</b>	Thunder Power ProLite 3S 1350 mAh

### B. Data Reduction

The data reduction technique used is based on previous works.<sup>22,23</sup> Additional data is required for analysis, beyond what was previously presented in earlier sections, including: propeller performance data for calculation of the lift and drag coefficient and pitch moment of inertia of the aircraft for calculation of the moment coefficient.

Data reduction starts with calculating the total external forces acting on the aircraft, which are a combination of the aerodynamic forces, thrust, and the gravitational force.

$$\mathbf{F}_{external} = \mathbf{F}_{aero} + \mathbf{F}_G + \mathbf{F}_T \quad (1)$$

By subtracting the gravitational force  $\mathbf{F}_G$  and the thrust  $\mathbf{F}_T$  from the total external forces, the aerodynamic forces can be found.

$$\mathbf{F}_{aero} = \mathbf{F}_{external} - \mathbf{F}_G - \mathbf{F}_T \quad (2)$$

where  $\mathbf{F}_G$  is

$$\mathbf{F}_G = mg [-\sin \theta \quad \sin \phi \cos \theta \quad \cos \phi \cos \theta]^T \quad (3)$$

The thrust is calculated from the airspeed and rotation rate, given knowledge of the propeller's performance curves. Such curves can be found through propeller testing<sup>35,36</sup> or in existing databases.<sup>37</sup>

The total external forces acting on the aircraft can be found by multiplying the mass of the aircraft by the body-fixed axes accelerations ( $a_x, a_y, a_z$ ), which are given by the IMU.

$$\mathbf{F}_{external} = [ a_x \ a_y \ a_z ]^T m \quad (4)$$

The body frame components of the aerodynamic force  $\mathbf{F}_{aero}$  are defined as ( $F_x, F_y, F_z$ ). These components are transformed into the wind frame to yield expressions for lift and drag.

$$L = -F_z \cos \alpha + F_x \sin \alpha \quad (5a)$$

$$D = -F_z \sin \alpha \cos \beta - F_x \cos \beta \cos \alpha - F_y \sin \beta \quad (5b)$$

where  $\alpha$  and  $\beta$  are

$$\alpha = \tan^{-1}(w/u) \quad (6a)$$

$$\beta = \sin^{-1}(v/V) \quad (6b)$$

The body-frame true velocities are found by performing inertial to body frame rotations

$$\begin{bmatrix} u \\ v \\ w \end{bmatrix} = R_I^B(\phi, \theta, \psi) \begin{bmatrix} v_x \\ v_y \\ v_z \end{bmatrix} \quad (7)$$

where,

$$R_I^B(\phi, \theta, \psi) = \begin{bmatrix} 1 & 0 & 0 \\ 0 & \cos \phi & \sin \phi \\ 0 & -\sin \phi & \cos \phi \end{bmatrix} \begin{bmatrix} \cos \theta & 0 & -\sin \theta \\ 0 & 1 & 0 \\ \sin \theta & 0 & \cos \theta \end{bmatrix} \begin{bmatrix} \cos \psi & \sin \psi & 0 \\ -\sin \psi & \cos \psi & 0 \\ 0 & 0 & 1 \end{bmatrix} \quad (8)$$

It should be noted that wind corrections must be applied between the ground velocities and true velocities. The lift and drag coefficients are then found.

$$C_L = \frac{2L}{\rho V^2 S} \quad (9a)$$

$$C_D = \frac{2D}{\rho V^2 S} \quad (9b)$$

Similarly to the total external forces acting on the aircraft, the pitching moment is found based on the pitch moment of inertia and the pitch angular acceleration.

$$\mathbf{M} = I_{yy} \dot{q} \quad (10)$$

The moment coefficient is then found

$$C_M = \frac{2M}{\rho V^2 S c} \quad (11)$$

At the time of paper submission, the pitch moment of inertia data for the aircraft was not available. A moment of inertia testing apparatus is in the process of being designed, constructed and tested, and will be presented in future work. As such, the moment coefficient results for the flight test are not presented in this paper.

## C. Results

During flight testing, the aircraft was flown through several low speed powered stalls in order to attempt to sweep the angle of attack of the aircraft. For this flight testing maneuver, the throttle was maintained above idle. The maneuver was performed by pitching the aircraft up to approximately 30 deg with the elevator, then all controls were centered, allowing the aircraft to transition through the partial stall. Due to the view point of the pilot on the ground, the aircraft entered the maneuver with a roll angle of around 35 degrees, which caused the aircraft to sideslip; the sideslip decreased as the dihedral leveled the aircraft off through the maneuver, though overshoot. The motion of the recovery was recorded in order to provide a broad sweep of angles-of-attack at a relatively low rotation rate. State data of the recovery is presented in Fig. 18.

As the control surfaces were centered throughout the maneuver, the range of angles-of-attacks achieved were limited, specifically between -2 to 7 degs. In a similar manner, the total velocity the aircraft settled at throughout the maneuver was 16 m/s (36 mph). Fig. 19 shows the lift and drag coefficients from the maneuver. As mentioned in the previous section, the moment coefficient could not be calculated as the pitch moment of inertia data for the aircraft was not available at the time of paper submission. The stability derivatives of the lift and drag coefficients were calculated using data from -2 to 2 deg, which appear to be linear. The stability derivatives are tabulated as follows.

$$\begin{aligned} C_{L_\alpha} &= 0.0606 & C_{L_0} &= 0.5345 \\ C_{D_\alpha} &= 0.00237 & C_{D_0} &= 0.0489 \end{aligned}$$

## VI. Results Comparison

The results from each of the analysis are tabulated in Table 6. The low order tools and CFD results predicted lift curve slope and zero angle-of-attack values within the same order of magnitude of the flight test and had similar trends. Ansys had the closest lift curve slope to the flight test, which may be attributed to 3D effects not accounted for in the low order tools, as XFLR5 and AVL had similar predictions. The drag predictions from AVL were lower than those from experimental data, XFLR5 and Ansys, which was attributed to how AVL does not include viscous effects. The drag predicted from Ansys Fluent is the closest to the to flight test data results although the drag curve slope for XFLR5 and Ansys Fluent were lower than the experimental results by an order of magnitude.

**Table 6. Aircraft characteristics and stability derivatives for each analysis run**

	<b>XFLR5</b>	<b>AVL</b>	<b>Ansys Fluent</b>	<b>Flight Test</b>
$C_{L_\alpha}$	0.0827	0.0810	0.0667	0.0606
$C_{D_\alpha}$	0.0075	0.0043	0.0067	0.0237
$C_{M_\alpha}$	-0.0249	-0.0193	-0.0340	–
$C_{L_0}$	0.357466	0.33088	0.3875	0.5345
$C_{D_0}$	0.020282	0.00633	0.05512	0.0489
$C_{M_0}$	-0.00799	-0.06364	-0.00659	–

The zero angle-of-attack moments predicted by XFLR5 and Ansys are very close though their slopes are within the same order of magnitude, whereas the moment predicted by AVL is greater than the previous solutions by an order of magnitude, which can also be attributed to viscous effects. The moment curve slopes from all three of the tools were within the same order of magnitude. The differences between the moment slopes could be attributed to viscous and 3D effects as the angle-of-attack increases, which will limit the the low order results to small angles-of-attack. The zero angle-of-attack moment from XFLR5 and Ansys are of the same order of magnitude, whereas the AVL results are greater by an order of magnitude. The difference in AVL moment results can be attributed to the lack of viscous effects in the calculations as drag contributes to the moment acting upon the aircraft.

As the aircraft was trimmed during the flight test, it was very difficult to accurately determine the zero angle-of-attack coefficients, especially as the trim values shifted. Although the zero angle-of-attack coefficients did not match the experimental results, the lift curve slopes computed from Ansys and the flight test were very close. As the zero lift coefficient derived from the flight test is higher than the CFD solution, the elevator control surfaces most likely were trimmed away from the center.

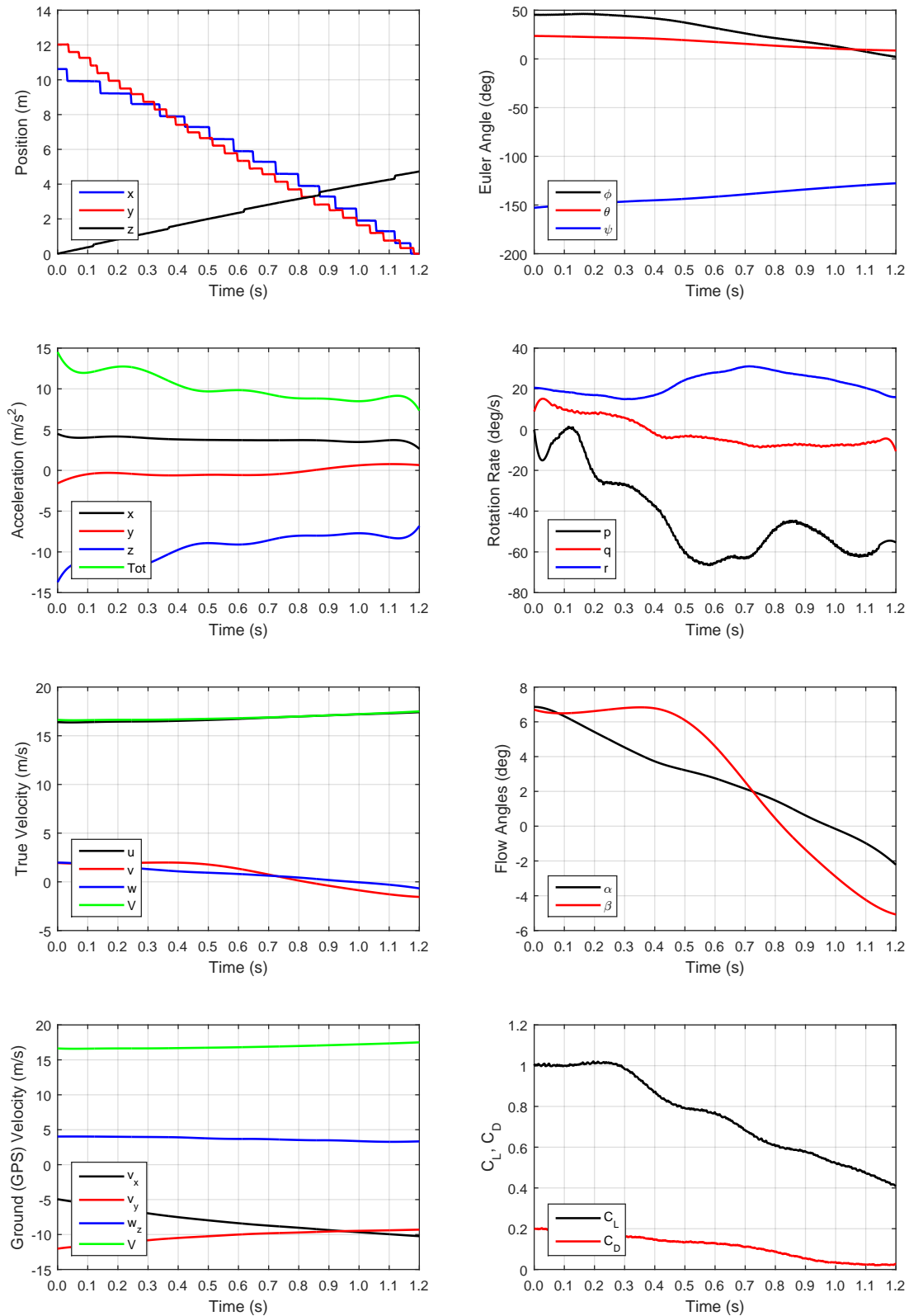


Figure 18. A time history of aircraft state during a stall.

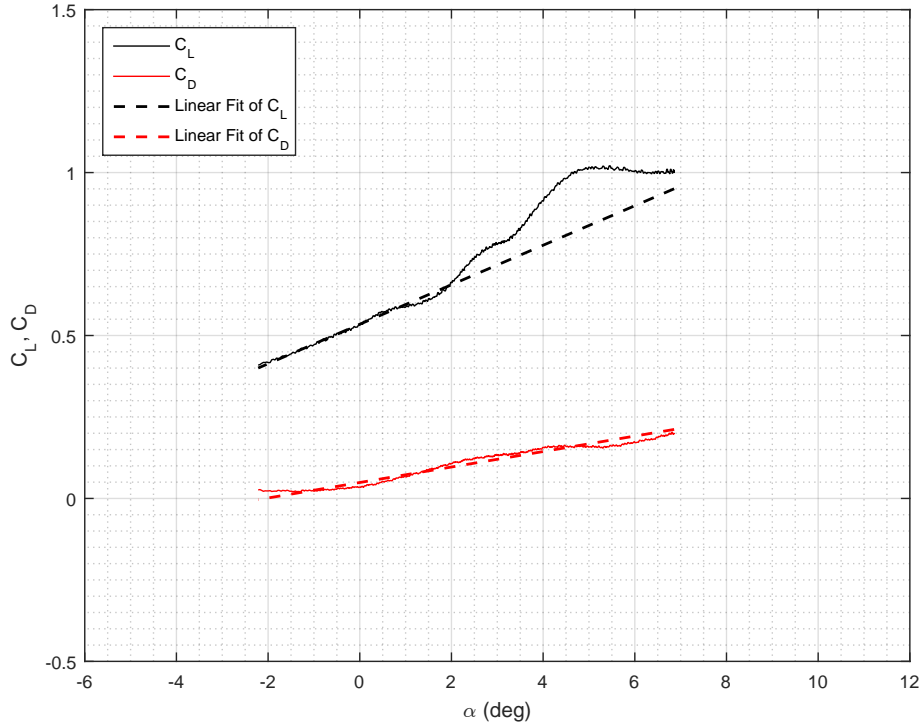


Figure 19. Flight testing lift, drag, and moment coefficients vs. angle of attack for the Avistar UAV at 16 m/s

## VII. Summary and Future Work

This paper discussed and compared several computational tools used to determine the aerodynamic characteristics of an unmanned aircraft with experimental results obtained from flight testing. Two low-order computational tools based on lifting-line theory, XFLR5 and AVL, and one high-order method, using Ansys Fluent, were presented. A 62.5 in. wingspan fixed-wing unmanned aircraft, which had previously been 3D scanned, was used as the aircraft for comparison purposes. Detailed geometry data was created from the 3D scan point cloud and was input into the computational tools.

The lift, drag, and moment coefficient results from the computational tools were presented, showing similarity among themselves, and were compared to experimental flight testing results. The computational lift results were similar to those from the flight testing results. The flight testing drag was greater in both slope and zero angle-of-attack value in comparison to the computation results as was expected. The computational moment coefficient could not be compared to experimental results as the aircraft longitudinal moment of inertia was not known at the time of publication.

Future work would begin by measuring the moment of inertia of the aircraft, which would allow the experimental pitching moment coefficients to be calculated and compared to the computational results. Additionally, both the computational and flight test results could be expanded to also including lateral and vertical stability characteristics. A further extension could look at using the computational tools and flight testing to determine and compare control derivative characteristics for both trim and control deflections about all three axes.

Furthermore, future work could also include enhancements to the methods used. In the scope of CFD, different turbulence models could be used and compared. For AVL, although the tool cannot capture viscous effects, a constant pressure drag could be included into the input file; however, this term would need to be determined independently. Flight testing could be automated to increase the precision of the maneuvers performed and generate consistent results between multiple flight tests.

## Acknowledgments

The authors would like to thank Prof. Marco Caccamo in the Department of Computer Science at University of Illinois at Urbana-Champaign for offering access to the computational resources used in this work. Additionally, the authors would also like to thank Richard Nai, Mirco Theile, and Hoong Chieh Yeong for their help with flight testing. Finally, authors owe thanks to Renato Mancuso from Al Volo for providing integration and operation support.

## References

- <sup>1</sup>Andre Deperrois, “XFLR5,” <http://www.xflr5.com/>, Accessed Jun. 2017.
- <sup>2</sup>Mark Drela, “AVL,” <http://web.mit.edu/drela/Public/web/avl/>, Accessed Jun. 2017.
- <sup>3</sup>Mark Drela, “XFOIL,” <http://web.mit.edu/drela/Public/web/xfoil/>, Accessed Jun. 2017.
- <sup>4</sup>Dantsker, O. D., “Determining Aerodynamic Characteristics of an Unmanned Aerial Vehicle using a 3D Scanning Technique,” AIAA Paper 2015-0026, AIAA Aerospace Sciences Meeting, Kissimmee, Florida, Jan. 2015.
- <sup>5</sup>University, P., *XFLR5 Analysis of foils and wings operating at low Reynolds numbers*, 2009.
- <sup>6</sup>Maskew, B., “Program VSAERO Theory,” Tech. rep., NASA Contractor Report 4023, 1987.
- <sup>7</sup>Perry, J., Mohamed, A., Johnson, B., and Lind, R., “Estimating Angle of Attack and Sideslip Under High Dynamics on Small UAVs,” Proceedings of the ION-GNSS Conference, Savannah, Georgia, 2008.
- <sup>8</sup>Johnson, B. and Lind, R., “High Angle-of-Attack Flight Dynamics of Small UAVs,” AIAA Paper 2009-61, AIAA Aerospace Sciences Meeting, Orlando, Florida, Jan. 2009.
- <sup>9</sup>Johnson, B. and Lind, R., “Characterizing Wing Rock with Variations in Size and Configuration of Vertical Tail,” AIAA Paper 2009-6151, AIAA Atmospheric Flight Mechanics Conference, Chicago, Illinois, Aug. 2009.
- <sup>10</sup>Johnson, B. and Lind, R., “Characterizing Wing Rock with Variations in Size and Configuration of Vertical Tail,” *Journal of Aircraft*, Vol. 47, No. 2, 2010, pp. 567–576.
- <sup>11</sup>Saha, B., Koshimoto, E., Quach, C. C., Hogge, E. F., Strom, T. H., Hill, B. L., Vazquez, S. L., and Goebel, K., “Battery Health Management System for Electric UAVs,” IEEE Aerospace Conference, Big Sky, Montana, 2011.
- <sup>12</sup>Ippolito, C., Yeh, Y. H., and Kaneshige, J., “Neural Adaptive Flight Control Testing on an Unmanned Experimental Aerial Vehicle,” AIAA Paper 2007-2827, AIAA Infotech@Aerospace, Rohnert Park, California, May 2007.
- <sup>13</sup>Jordan, T. L. and Bailey, R. M., “NASA Langley’s AirSTAR Testbed: A Subscale Flight Test Capability for Flight Dynamics and Control System Experiments,” AIAA Paper 2008-6660, AIAA Atmospheric Flight Mechanics Conference, Honolulu, Hawaii, Aug. 2008.
- <sup>14</sup>Keshmiri, S., Leong, E., Jager, R., and Hale, R., “Modeling and Simulation of the Yak-54 Scaled Unmanned Aerial Vehicle Using Parameter and System Identification,” AIAA Paper 2008-6900, AIAA Atmospheric Flight Mechanics Conference, Honolulu, Hawaii, Aug. 2008.
- <sup>15</sup>Jones, V. A. and Keshmiri, S., “First Flight Risk Mitigation Related to Pilot Unfamiliarity with a New UAV Platform,” AIAA Paper 2010-3489, AIAA Infotech@Aerospace, Atlanta, Georgia, June 2010.
- <sup>16</sup>Lykins, R. and Keshmiri, S., “System Identification of a COTS Autopilot System Using Flight Test Data,” AIAA Paper 2010-7648, AIAA Atmospheric Flight Mechanics Conference, Toronto, Ontario, Canada, Aug. 2010.
- <sup>17</sup>Lykins, R. and Keshmiri, S., “Modal Analysis of 1/3-Scale Yak-54 Aircraft Through Simulation and Flight Testing,” AIAA Paper 2011-6443, AIAA Atmospheric Flight Mechanics Conference, Portland, Oregon, Aug. 2011.
- <sup>18</sup>Sebes, J., VanSlike, W., Williams, M., McCandless, S. E., Stastny, T., Worden, G., and Brunkhorst, N., “Flight Testing and Evaluation of the Structural Response to Flight Loads of a Small Scale Unmanned Aerial System,” AIAA Paper 2012-2498, AIAA Infotech@Aerospace, Garden Grove, California, June 2012.
- <sup>19</sup>Dantsker, O. D., Johnson, M. J., Selig, M. S., and Bretl, T. W., “Development of the UIUC Aero Testbed: A Large-Scale Unmanned Electric Aerobatic Aircraft for Aerodynamics Research,” AIAA Paper 2013-2807, AIAA Applied Aerodynamics Conference, San Diego, California, June 2013.
- <sup>20</sup>Ragheb, A. M., Dantsker, O. D., and Selig, M. S., “Stall/Spin Flight Testing with a Subscale Aerobatic Aircraft,” AIAA Paper 2013-2806, AIAA Applied Aerodynamics Conference, San Diego, California, June 2013.
- <sup>21</sup>Dantsker, O. D., Mancuso, R., Selig, M. S., and Caccamo, M., “High-Frequency Sensor Data Acquisition System (SDAC) for Flight Control and Aerodynamic Data Collection Research on Small to Mid-Sized UAVs,” AIAA Paper 2014-2565, AIAA Applied Aerodynamics Conference, Atlanta, Georgia, June 2014.
- <sup>22</sup>Dantsker, O. D. and Selig, M. S., “High Angle of Attack Flight of a Subscale Aerobatic Aircraft,” AIAA Paper 2015-2568, AIAA Applied Aerodynamics Conference, Dallas, Texas, Jun. 2015.
- <sup>23</sup>Dantsker, O. D., Ananda, G. K., and Selig, M. S., “GA-USTAR Phase 1: Development and Flight Testing of the Baseline Upset and Stall Research Aircraft,” AIAA Paper 2017-4078, AIAA Applied Aerodynamics Conference, Denver, Colorado, June 2017.
- <sup>24</sup>Blauwe, H. D., Bayraktar, S., Feron, E., and Lokumcu, F., “Flight Modeling and Experimental Autonomous Hover Control of a Fixed Wing Mini-UAV at High Angle of Attack,” AIAA Paper 2007-6818, AIAA Guidance, Navigation, and Control Conference, Hilton Head, South Carolina, Aug. 2007.
- <sup>25</sup>Frank, A., McGrewy, J. S., Valentiz, M., Levinex, D., and How, J. P., “Hover, Transition, and Level Flight Control Design for a Single-Propeller Indoor Airplane,” AIAA Paper 2007-6318, AIAA Guidance, Navigation, and Control Conference, Hilton Head, South Carolina, Aug. 2007.
- <sup>26</sup>Bilodeau, P. R., Poulin, E., Gagnon, E., Wong, F., and Desbiens, A., “Control of a Hovering Mini Fixed Wing Aerial Vehicle,” AIAA Paper 2009-5794, AIAA Guidance, Navigation and Control Conference, Chicago, Illinois, Aug. 2009.

<sup>27</sup>Uhlig, D., Sareen, A., Sukumar, P., Rao, A. H., and Selig, M. S., “Determining Aerodynamic Characteristics of a Micro Air Vehicle Using Motion Tracking,” AIAA Paper 2010-8416, AIAA Guidance, Navigation, and Control Conference, Toronto, Ontario, Canada, Aug. 2010.

<sup>28</sup>ZCorporation, “The New ZScanner 800,” [www.zcorp.com/documents/182\\_ZScanner800-tearsheet-v05wb.pdf](http://www.zcorp.com/documents/182_ZScanner800-tearsheet-v05wb.pdf), Accessed Mar. 2013.

<sup>29</sup>Hobbico, Inc., “Great Planes Avistar Elite .46 Advanced Trainer RTF,” <http://www.greatplanes.com/airplanes/gpma1605.html>, Accessed Oct. 2013.

<sup>30</sup>Mancuso, R., Dantsker, O. D., Caccamo, M., and Selig, M. S., “A Low-Power Architecture for High Frequency Sensor Acquisition in Many-DOF UAVs,” Submitted to International Conference on Cyber-Physical Systems, Berlin, Germany, April 2014.

<sup>31</sup>Al Volo LLC, “Al Volo: Flight Data Acquisition Systems,” <http://www.alvolo.us>, Accessed Jun. 2017.

<sup>32</sup>UIUC Applied Aerodynamics Group, “UIUC Airfoil Coordinates Database,” [http://aerospace.illinois.edu/m-selig/ads/coord\\_database.html](http://aerospace.illinois.edu/m-selig/ads/coord_database.html).

<sup>33</sup>Andre Deperrois, “F.A.Q : Why do I get the message ”Point is out of the flight envelope ?”,” [http://www.xflr5.com/docs/Point\\_Out\\_Of\\_Flight\\_Envelope.pdf](http://www.xflr5.com/docs/Point_Out_Of_Flight_Envelope.pdf), Accessed Dec. 2013.

<sup>34</sup>ANSYS, Inc, “ANSYS Fluent: CFD Simulation,” <http://www.ansys.com/Products/Fluids/ANSYS-Fluent>, Accessed Jun. 2017.

<sup>35</sup>Brandt, J. B. and Selig, M. S., “Propeller Performance Data at Low Reynolds Numbers,” AIAA Paper 2011-1255, AIAA Aerospace Sciences Meeting, Orlando, Florida, Jan. 2011.

<sup>36</sup>Dantsker, O. D., Selig, M. S., and Mancuso, R., “A Rolling Rig for Propeller Performance Testing,” AIAA Paper 2017-3745, AIAA Applied Aerodynamics Conference, Denver, Colorado, Jun. 2017.

<sup>37</sup>UIUC Applied Aerodynamics Group, “UIUC Propeller Database,” <http://m-selig.ae.illinois.edu/props/propDB.html>.